Carbohydrate Polymers 335 (2024) 122089

Contents lists available at ScienceDirect

Carbohydrate Polymers

journal homepage: www.elsevier.com/locate/carbpol

Crystalline nanoxylan from hot water extracted wood xylan at multi-length scale: Molecular assembly from nanocluster hydrocolloids to submicron spheroids

Yidong Zhang [a], Luyao Wang [a], Hao Zhang [a], Emil Rosqvist [b], Mika Lastusaari [c], Jouko Peltonen [b], Lari Vähäsalo [a,d], Chunlin Xu [a], Xiaoju Wang [a,*], Andrey Pranovich [a,*]

[a] Laboratory of Natural Materials Technology, Åbo Akademi University, Henrikinkatu 2, FI-20500 Turku, Finland
[b] Physical Chemistry, Laboratory of Molecular Science and Engineering, Åbo Akademi University, Henrikinkatu 2, Turku FI-20500, Finland
[c] Department of Chemistry, University of Turku, FI-20014 Turku, Finland
[d] CH-Bioforce Oy, Espoo FI-02170, Finland

ARTICLE INFO

Keywords:
Xylan
Crystalline nanoxylan
Nanocluster hydrocolloids
Bio-based nanomaterials
Phosphorescence

ABSTRACT

As a contribution to expand accessibility in the territory of bio-based nanomaterials, we demonstrate a novel material strategy to convert amorphous xylan preserved in wood biomass to hierarchical assemblies of crystalline nanoxylan on a multi-length scale. By reducing the end group in pressurized hot water extracted (PHWE) xylan to primary alcohol as a xylitol form with borohydride reduction, the endwise-peeling depolymerization is effectively impeded in the alkali-catalyzed hydrolytic cleavage of side substitutions in xylan. Nanoprecipitation by a gradual pH decrease resulted in a stable hydrocolloid dispersion in the form of worm-like nanoclusters assembled with primary crystallites, owing to the self-assembly of debranched xylan driven by strong intra- and inter-chain H-bonds. With evaporation-induced self-assembly, we can further construct the hydrocolloids as dry submicron spheroids of crystalline nanoxylan (CNX) with a high average elastic modulus of 47–83 GPa. Taking the advantage that the chain length and homogeneity of PHWE-xylan can be tailored, a structure-performance correlation was established between the structural order in CNX and the phosphorescent emission of this crystalline biopolymer. Rigid clusterization and high crystallinity that are constructed by strong intra- and intermolecule interactions within the nanoxylan effectively restrict the molecular motion, thereby promoting the emission of ultralong organic phosphorescence.

1. Introduction

Renewable natural polysaccharides are of abundant availability and have been largely applied in various fields, such as food packaging, cosmetics, personal care/sanitary products, and biomedical, due to their inherent low toxicity, biodegradability, and biocompatibility (Aliev et al., 2009; Cheng et al., 2021; Qi et al., 2021). Driven by the urgent need for bio-based products to replace petroleum-based counterparts in the societal sustainability transformation, nanostructured polysaccharides are certain to be a mainstay of the forthcoming green materials revolution (Rao, Lv, Chen, & Peng, 2023; Su et al., 2021). These bio-based nanomaterials exhibit nano-specific properties, such as high specific surface area leading to increased interfacial reactivity, high aspect ratio and crystallinity providing strength and stiffness, and even new quantum effects (Ghasemlou, Daver, Ivanova, Habibi, & Adhikari, 2021; Thomas et al., 2018). Manufactured from forestry-, crop-, or crustaceans-residual stream, nanocellulose, and nanochitin are currently the most studied nanostructured polysaccharides, which are produced top-down by selectively carving the segmented mesoarchitecture from the macromolecular assemblies built by nature as an elementary semi-crystalline nanofibril (Bai et al., 2022; Habibi, Lucia, & Rojas, 2010). These nanomaterials preserve, to some degree, the biological morphology of the elementary nanofibril, thereby inheriting excellent toughness and resistance. Xylan is the third most abundant polysaccharide in nature after cellulose and chitin, accounting for approximately one-third of all renewable organic carbon on Earth

* Corresponding authors at: Laboratory of Natural Materials Technology, Faculty of Science of Engineering, Åbo Akademi University, Henrikinkatu 2, Turku FI-20500, Finland.
E-mail addresses: xwang@abo.fi (X. Wang), andrey.pranovich@abo.fi (A. Pranovich).

https://doi.org/10.1016/j.carbpol.2024.122089
Received 8 January 2024; Received in revised form 11 March 2024; Accepted 24 March 2024
Available online 26 March 2024

(Urbanowicz, Peña, Moniz, Moremen, & York, 2014). In contrast to the crystalline nature of linear cellulose and chitin, xylan is an amorphous acetylated and branched biopolymer. The native form of xylan comprises a conserved backbone of β-(1,4)-linked D-xylose units with side branches. The composition of xylan varies considerably among plant species, e.g., 4-*O*-methylglucuronoxylans are the primary components of hemicellulose as found in hardwoods, while arabino-4-*O*-methylglucuronoxylans are abundant in softwoods and grasses (Bosmans et al., 2014; Ebringerova & Heinze, 2000). Importantly, part of the xylose units are acetylated, which impairs the intra- and inter-chain hydrogen bonding among the macromolecules of xylan itself (Andrewartha, Phillips, & Stone, 1979; Benouadah, Pranovich, Aliouche, Labidi, & Willfor, 2021). Thus, native xylan exists as amorphous but is tightly associated with the cellulose microfibrils to together structure the plant cell wall (Roubroeks & Kondo, 2012). To expand the accessibility of the landscape of bio-based nanomaterials, manufacturing nanoxylan, especially in a crystalline form, has been an intense research horizon in most recent years (Hao et al., 2021; Hao et al., 2022; Meng et al., 2021; Wang et al., 2023; Wang & Xiang, 2021).

The observation of xylan crystalline structure dated back to the 1940s, when xylose-based aggregates were isolated in small amounts from the black liquor of kraft wood pulping (Yundt, 1949). The close structural analogy between cellulose and xylan has long been emphasized and the crystallographic feature of xylan hydrate was of academic interest already several decades ago (Horio & Imamura, 1964; Nieduszynski & Marchessault, 1972). Compared with cellulose, the absence of the $–CH_2OH$ group on C_5 reduces the intermolecular 'reach' of xylan so that water is required to stabilize the lattice structure. The xylan crystal has a hexagonal crystal lattice of the unit cell of xylan hydrate as reflected by X-ray diffraction (Nieduszynski & Marchessault, 1972). The crystallinity of xylan was in general considered largely affected by the substitute sugar residues, i.e., glucuronic acid (GlcA) sidechains, 4-*O*-methylglucuronic acid (4-*O*-MeGlcA) sidechains, or arabinose sidechains, which are attached to the skeletal chains of xylose (Ebringerová, Hromádková, & Heinze, 2005). On this perspective, the sidechain elimination of bulky moieties of uronic acids to an extreme limit was earlier agreed as indispensable for obtaining the crystalline particles. This also accounts for the popularity of the *esparto* plant as the origin for investigation of crystalline xylan, as the xylan macromolecule from it contains few to no uronic acid sidechain as well as no arabinose sidechain, which otherwise is typical of other grasses (Chanda, Hirst, Jones, & Percival, 1950). Recently, Johnson et al. have concluded that the removal of sidechain uronic acids is not a necessity for the xylan macromolecule to form crystallinity by comparing the nanoxylan derived from wild-type *Arabidopsis* having sidechains with the one derived from a corresponding mutant plant lacking sidechains (Johnson et al., 2023). Through a controlled nucleation process by cooling down from a supersaturated condition, the xylan from wild-type *Arabidopsis* with sidechains could readily self-assemble as crystalline nanoxylan with a submicron diameter. Whereas, the xylan from the *Arabidopsis* mutant without sidechains interestingly formed spherulitic superstructures up to several microns, which could be subsequently fragmented into crystallites measuring 46 nm by 27 nm to yield hydrocolloids by sonication (Johnson, Mottiar, et al., 2023). This intercomparison also strongly implies that the side uronic acid units could interrupt the close packing of xylan chains in the crystal lattice and impede crystal growth.

To date, the manufacturing of wood nanoxylan has mainly used sidestream xylans that are extracted in cellulose fiber-first processes. For instance, several studies reported by Peng et al. have used the byproduct xylan that is extracted in a highly concentrated alkaline wood pulping process from a viscose mill to manufacture nanoxylans (Hao et al., 2021; Hao et al., 2022; Wang et al., 2023). Under such reaction conditions in kraft pulping, a significant portion of side-sugar units and almost all acetyl groups are to a large extent cleaved from the main chain of xylan polymer, and part *4-O*-MeGlcA as side-sugar units convert into the corresponding unsaturated hexane uronic acid by the loss of methanol during the alkaline pulping (Gellerstedt & Li, 1996; Gomes, de Sousa, Belenkiy, & Evtuguin, 2020; Pinto, Evtuguin, & Neto, 2005). Such a low-branched and deacetylated xylan biopolymer leads to closer inter−/intramolecular interactions and enables ordered arrangement of macromolecules driven by the strong intra- and inter-chain hydrogen bonds, thus presenting crystallinity (Nishiyama, 2018). Top-down methods, such as mild ammonium persulfate oxidation or sodium periodate oxidation in conjugation with subsequent ultrasonic treatment, have been successful in converting this crystalline xylan biopolymer to nanoxylans (Hao et al., 2022; Wang et al., 2023; Wang & Xiang, 2021). However, the native xylan is conceived to endure severe degradation via primary peeling reactions under harsh alkaline conditions, and that only small portions can survive as a polymeric form (Scheme 1). Thus, the efficiency of utilizing the native xylan in wood biomass to produce crystalline nanoxylan is not yet optimal with the current-existing processes.

In a modern biorefinery pilot, pressurized hot-water extraction (PHWE) of biomass feedstock at an elevated temperature and pressure can effectively isolate structural hemicelluloses in polymeric forms with high yields (Pranovich, Holmbom, & Willfor, 2016). Xylan from the PHWE process is close to native xylan with the side-sugar units and the acetyl groups preserved and has a high yield. To establish a viable route for manufacturing nanomaterials out of the PHWE-xylan is of high relevance for exploiting its high value-added applications, aiming to increase the economic feasibility of this biorefinery. As discussed above, xylans readily self-assemble into crystal hydrates in case the biopolymer is less branched and deacetylated. However, the sidechain moieties of GlcA and 4-*O*-MeGlcA on xylan are known recalcitrant even during hydrolysis at 121 °C and 15 psi in water (Fry, 1988). Under alkaline conditions, the hydrolytic action of alkali results in the side-chain removal but simultaneously causes peeling endwise of the main polymeric chain (Wang, Azhar, Lindstrom, & Henriksson, 2015). There, the main challenge is to avoid the depolymerization of the mainchain xylan, in the meantime debranching the side units and removing the acetyl groups. The successful elimination of side units is hypothesized to contribute to close packing of xylan chain and crystal growth. To this end, we adopt a protecting strategy to reform the reducing end-groups in the PHWE-xylan prior to alkaline debranching and deacetylation, which is effective in preventing the main-chain peeling and depolymerization. Thus, the PHWE-xylan could be tailored to almost linear xylan polymer, and further be processed via nanoprecipitation, resulting in the self-assembly of polymeric xylan in the form of closely packed nanocluster hydrocolloids. The as-proposed approach to utilize the PHWE-xylan in the preparation of nanoxylan was schematically compared to other strategies that utilize alkaline-extracted bioproduct xylan for the same purpose in Scheme 1.

As the PHWE-xylan is preserved as being acetylated, which is aqueous processable with membrane ultrafiltration to yield fractioned xylan with controlled molecular weight and narrow molecular weight dispersity ($Đ$). Taking this advantage, we tailor-make the PHWE-xylan fractions and correlate the macromolecular structure with the physical properties (i.e., the structural order and crystallinity) of the nanoxylans manufactured through the self-assembly of the deacetylated and debranched xylan fraction, and we aim to establish a structure-performance correlation between the structural order within the nanoxylan and the phosphorescent emission of this crystalline biopolymer.

Like native cellulose or chitin, the macromolecular assembly fosters its ability to structure into hierarchical assemblies spanning the nano- and macroscales. Research endeavors have also investigated the multiscale control over the morphology of the self-assembled xylan and its crystal growth. Zhang et al. subjected the *esparto* xylan to supersaturation under elevated temperate and pressure (120 °C in closed vessel) and subsequently recrystallized it under controlled cooling to fabricate xylan micro/nanoparticles with a diameter ranged in 400 nm – 2.5 μm (Zhang et al., 2023). The molecular solvent is recognized to play a significant role in the crystallization of xylan when processed from the wet to dry

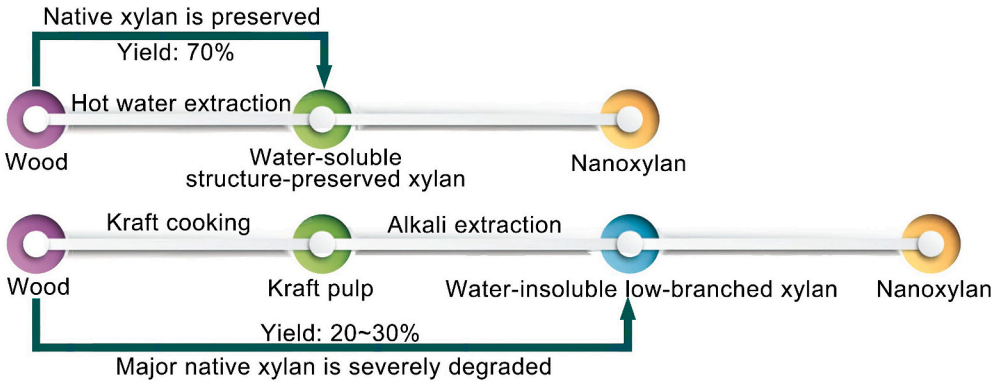

Scheme 1. Comparison of the preparation of CNX using water-soluble PHWE-xylan in this work with other strategies using alkaline-extracted side-stream xylan.

state. Hao et al. confirmed that the crystallinity of xylan was sensitive to hydration conditions (Hao et al., 2022). Johnson et al. reported that air-drying caused a 40 % decrease in height of xylan compared to wet particles, and xylan crystals lost crystallinity after vacuum drying, confirming the vital role of water in structuring the crystallinity (Johnson, Karaaslan, Cho, Ogawa, & Renneckar, 2023). Very intriguingly, Meng et al. used dimethyl sulfoxide (DMSO) to replace the H_2O in recrystallization process, leading to the formation of 2-fold helical structure in nanoxylan crystals (Meng et al., 2021). To this end, we also deployed the evaporation-induced self-assembly (EISA) method to assemble the nanocluster hydrocolloids to submicron spheroids of nanoxylan. Overall, our present research has established a proof-of-concept to convert the amorphous xylan that is extracted from hardwood biomass as a water-soluble polysaccharides to hierarchical assemblies of crystalline nanoxylan (CNX) as nanomaterials on a multi-scale.

2. Experimental section

2.1. Materials

$NaBH_4$ (≥98 %), NaOH (≥98 %), formic acid (98–100 %), methanol (≥99 %), ethanol (≥99.9 %), and glycerol (≥99 %) were purchased from Sigma-Aldrich. The chemical composition and molecular weight characteristics are listed in Table 1. All chemicals were used as received without any purification.

2.2. Exaction of native xylan and synthesis of CNX

Structure-preserved xylan preparation with natively occurred 4-*O*-methylglucuronic side units and the acetyl group was extracted from birch chips with pressurized hot-water extraction (PHWE) (max 150 °C) using pilot-scale batch extractor (Kilpeläinen, Kitunen, Pranovich, Ilvesniemi, & Willför, 2013; Lagerquist et al., 2019). The high-molecular-weight xylan fraction (H-xylan) and the low-molecular-weight xylan fraction (L-xylan) were further processed from the aqueous xylan PHWE extract using membrane ultrafiltration. The xylan fractions were precipitated with Ethanol/H_2O (85:15 %/v:v), filtrated and washed with EtOH, then vacuum-dried at 40 °C until constant weight. Major lignin impurities from xylan concentrates can be removed during Ethanol/H_2O precipitation, but small impurities of lignin in the precipitated xylans preparations were also detected.

CNX was prepared by alkaline treatment using the PHWE-xylan fractions as the starting material under the reformation of the reducing-end group by borohydride reduction to prevent the main-chain peeling. Briefly, 20 mg of $NaBH_4$, 15 mL of NaOH solution (1 M), and 1.5 g xylan powder were mixed and stirred in dark with N_2 purging overnight. After that, the mixture was transferred to reactor followed by reaction at 150 °C for various reaction times (4, 6, and 8 h). Then, the alkali-treated xylan solution was quantitatively transferred into a beaker and added 0.15 mL of glycerol, and the solution was neutralized with formic acid (1 wt%) to obtain precipitate. After that, the precipitate was washed four times by centrifugation (1096 ×*g*) with deionized water and methanol: H_2O (1:1/v:v) to obtain aqueous CNX dispersion. The yield of CNX was measured by the weight percentage of average values of triplicate batch of samples. Finally, a dialysis process was further deployed to remove impurities, and a white-turbid colloidal CNX dispersion was obtained.

2.3. Fabrication of crystalline submicron spheroids by self-assembly of CNX

EISA was conducted at different substrate surfaces for preparing crystalline submicron spheroids. The aqueous suspensions of CNX with a concentration of 0.01 wt% were carefully dropped on the substrate surfaces with different wettability (silicon or glass plate). After air-dried for 24 h, the self-assembled crystalline submicron spheroids were collected for further analysis.

Table 1
The chemical compositions and molecular weight characteristics of the starting PHWE-xylan fraction and CNX.

Samples	Composition (mg/g)										Molecular weight (kDa)		
	4-*O*-MeGlcA	Ara	Gal	GalA	Glc	GlcA	Man	Rha	Xylitol	Xyl	Mw	Mn	*Đ*
H-xylan	51.17	1.82	28.05	6.11	13.29	3.24	13.60	7.30	0.30	649.05	13.71	9.13	1.50
H-CNX-4 h	6.62	3.26	0.39	1.90	0.35	0.33	0.28	0.39	23.31	821.85	7.26	4.41	1.65
H-CNX-6 h	1.45	2.77	0.41	0.45	0.08	0.29	0.18	0.31	25.77	864.18	7.21	4.14	1.74
H-CNX-8 h	0.00	1.03	0.27	2.01	0.08	0.31	0.12	0.29	22.25	877.39	7.12	3.93	1.81
L-xylan	45.68	1.62	7.32	6.62	4.77	1.84	12.24	7.02	0.25	632.77	5.41	4.75	1.14
L-CNX-4 h	5.55	3.52	0.20	0.44	0.32	0.19	0.10	0.36	21.57	816.84	4.55	3.91	1.15
L-CNX-6 h	3.93	3.19	0.07	1.48	0.12	0.26	0.37	0.53	23.61	878.39	4.24	3.58	1.17
L-CNX-8 h	0.79	2.01	0.34	0.10	0.08	0.39	0.15	0.41	23.87	879.89	4.23	3.61	1.18

Note: 4-*O*-MeGlcA = 4-*O*-methylglucuronic acid; Ara = arabinose; Gal = galactose; GalA = galacturonic acid; Glc = glucose; GlcA = glucuronic acid; Man = mannose; Rha = rhamnose; Xyl: xylose.

2.4. Characterization

The sugar compositions of xylan and CNX were determined by acid methanolysis and followed GC equipped with a flame ionization detector. 0.5 mg of xylan or CNX sample was subjected to 2 mL of 2 M HCl in anhydrous methanol and treated at 105 °C for 3 h. The excess HCl was neutralized by adding 150 μL pyridine. The internal standard of 0.1 mg/mL (resorcinol in MeOH) was added to the sample. The sample was evaporated in a stream of nitrogen and further dried in a vacuum desiccator at 40 °C until dry. The sample was dissolved in 150 μL pyridine, and 150 μL hexamethyldisilane and 80 μL trimethylchlorosilane were added. The monosaccharides and uronic acids were silylated overnight at room temperature before GC analysis. The reported sugar compositions as anhydrosugar are the average values of triplicate measurements of samples.

High-performance size exclusion chromatograph (Agilent 1100 Series) equipped with an RI detector (Wyatt Technology Optilab High Concentration Differential Refractometer with a Laser Option 785 nm, Wyatt Technology, USA) and a MALS detector (Wyatt Technology DAWN 8 ambient with a Laser Option 785 nm, Wyatt Technology, USA) was applied to measure the molecular weight distribution of xylan and CNX samples. Xylan and CNX were washed with absolute ethanol and DMAc three times to remove water, then dissolved in DMAc/LiCl (9 %) to 20 mg/mL overnight. After fully dissolving, the transparent solution was diluted three times with DMAC/LiCl (0.9 %) eluent, followed by filtering with a nylon syringe filter (0.2 μm) before measurement. The reported molecular weight is the average value of duplicate measurements of samples.

Liquid state ^{1}H and ^{13}C NMR analysis of xylan and CNX samples were performed on a Bruker AVANCE III 500 MHz NMR spectrometer equipped with a CryoProbe at 298 K for 64 and 10,000 scans, respectively. The samples were dissolved in tetrabutylphosphonium acetate ($[P_{4444}][OAc]$): DMSO-d_6 (1:4 / w:w) to 50 mg/mL before NMR analysis. Solid state CP/MAS ^{13}C NMR of xylan and CNX samples were conducted on an Oxford 400 MHz NMR spectrometer operating at 298 K with a spinning rate of 14 kHz.

The steady state luminescence spectra were recorded with an Edinburgh Instruments FLS1000 spectrometer with a continuous wave 450 W Xe lamp (Xe_2) as the excitation source and a PMT-900 photomultiplier tube as the detector. The emission spectra presented here were recorded using 300 nm as the excitation wavelength. A 330 nm high-pass filter was used on the emission side to suppress the reflected excitation beam. Phosphorescence spectra were recorded with a Varian Cary Eclipse Fluorescence Spectrophotometer equipped with a Hamamatsu R928 PMT and a pulsed 150 W Xe lamp. Afterglow fading curves were recorded in 1 s intervals with a Hagner ERP-105 luminance photometer after a 2 min exposure to a 6 W 302 nm UV lamp (UVM-57). The UV lamp was operated at a 4.3 mW/cm^2 irradiance as measured by an Opsytec Dr.Gröbel Radiometer RM 12 equipped with an RM12 sensor calibrated for UVB. All measurements were done at room temperature. Photos and videos were obtained under and after irradiation with the same 302 nm UV lamp described above. The camera was Canon EOS 250D.

Detailed information regarding instrumental setups and experimental procedures for Raman spectroscopy, X-ray diffraction analysis (XRD), differential scanning calorimetry (DSC) and thermogravimetric analysis (TGA), transmission electron microscopy (TEM), scanning electron microscope (SEM), atomic force microscopy (AFM), and zeta potential employed for PHWE-xylan and CNX characterizations are given in the Supporting information.

3. Results and discussion

3.1. Reducing end protection and alkali-catalyzed hydrolytic cleavage of side substitutions to convert PHWE-xylan as a linear biopolymer

As illustrated in Fig. 1a and Scheme 1, our two-stage synthesis route is an endeavor to convert amorphous xylan to CNX. We strategically combined the PHWE biorefinery with the hydrolytic debranching to yield linear xylan polymer, and at last deployed the nanoprecipitation approach to yield CNX. For the hydrolytic cleavage of side substitutions in the acetylated xylan, both acid and alkali can catalyze the reaction. Acid-catalyzed hydrolytic cleavage is not selective and causes a random depolymerization of the main chain (Vibert, Fayolle, Ricard, & Dupont, 2023). In contrast, alkali-catalyzed hydrolytic cleavage removes the side chains but simultaneously induces the endwise peeling reaction (Y. Wang et al., 2015). Therefore, a reduction treatment of xylan with sodium borohydride ($NaBH_4$) under an alkaline condition was at first carried out at room temperature to reduce the terminal sugar unit on the reducing end. Subsequently, the debranching and deacetylation were continued with one-pot reaction by elevating the temperature to 150 °C for a reaction duration of 4 h, 6 h, or 8 h. After cooling to room temperature, glycerol was introduced to react with the residual borohydride towards the evolution of hydrogen gas and the formation of borate, which can readily eliminate the hazards associated with borohydride. The as-prepared product was neutralized by adding formic acid solution (1 wt%) drop by drop to induce a gradual pH change of the product shifting from alkaline towards neutral. The sediments were centrifuged and purified with several wash cycles with methanol: H_2O (1:1/v:v) and deionized water. Eventually, a water dialysis process was deployed to remove impurities, and the final product of CNX is a white-turbid colloidal dispersion of insoluble nanoclusters of xylan (Figs. 1a and S1), as it was later verified in material characterizations. As a control, the synthesis was carried out without the borohydride reduction to the reducing ends, and then only a deep brown solution was obtained in the alkali-catalyzed hydrolysis reaction for 4 h (Fig. S2). Not surprisingly, no solid product was received after the washing steps, because the endwise peeling reaction induced severe main-chain degradation of the polymeric PHWE-xylan when the reducing ends were not reformed. The mechanistic hypothesis is confirmed that the reduction of the terminal sugar unit as a xylitol unit could protect the main chain by inhibiting the alkali-induced peeling in the corresponding fragments (Fig. 1b). After the alkaline treatment, the side substitutions (both side-sugar units and acetyl groups) were removed, and the linear xylan polymer could align and pack to form crystalline structures by self-assembly due to the presence of strong intra- and inter-molecular interactions, i.e., *van der Waals* forces and H-bonds.

To consolidate the above-mentioned hypothesis, the chemical composition and molecular weight of nanoxylans prepared from the H-xylan and L-xylan were analyzed to reveal the structural changes of xylan before and after the alkali-catalyzed hydrolysis reaction. As shown in Table 1, the content of side uronic acid unit (i.e., 4-*O*-MeGlcA) of hardwood-xylan gradually decreased to be very low or eventually even non-detectable by GC at applied conditions for 4-*O*-MeGlcA as the reaction time increased from 4 h to 8 h, and the content of xylose in the end product gradually increased with respect to that in the starting xylan fraction. Consequently, the content of xylose unit in the xylan polymer increased from 60 to 65 wt% for the starting PHWE-xylan to above 90 wt % for the CNXs-8 h. These results indicate that the side-chain removal effect is significant under the designated conditions and an almost linear polysaccharide mainly composed of xylose unit is fabricated. More importantly, the xylitol content in all debranched xylans, when compared to the starting xylan fractions, was drastically increased, confirming the reduction of the end group in xylan chain to a primary alcohol. Furthermore, the average molecular weight (Mw) and the number average molecular weight (Mn) of xylans decreased after the alkali-catalyzed hydrolysis reaction, e.g., the Mn of H-xylan decreased

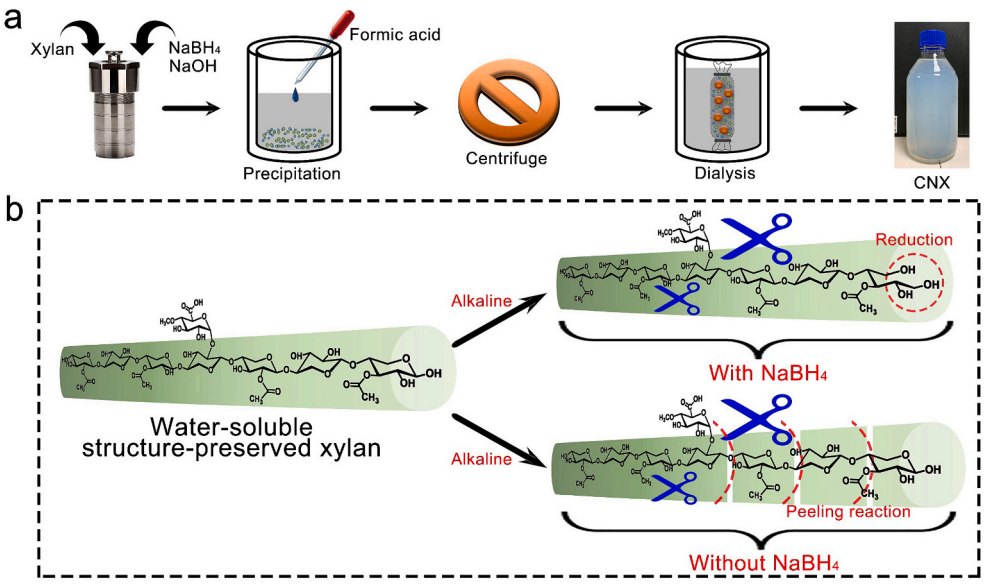

Fig. 1. Design strategy of xylan nanocluster hydrocolloids: (a) preparation of the colloidal CNX dispersion by reducing-end reformation and deacetylation/debranching xylan under alkaline conditions followed by dialysis. (b) Schematic illustration of the protection effect of converting the reducing end of xylan as primary alcohol by borohydride reduction and the peeling effect in alkaline conditions without reducing-end reformation.

from 9.13 kDa to 3.93 kDa, and the Mn of L-xylan decreased from 4.75 kDa to 3.61 kDa (Table 1). Nevertheless, the nanoxylans remain in a polymeric form according to the molecular weight attributes, ascribed to the great effort in protecting the reducing end from peeling. Meanwhile, the $Đ$ value of L-CNXs is noted to be smaller than that of H-CNXs. This suggests that the L-CNX is composed of short and homogeneous xylan chains, as the corresponding fraction has a narrower distribution after the membrane-based ultrafiltration. These differences on the chain length and homogeneity of xylan turn out to be of high relevance for controlling the size and crystalline features of nanoxylan.

Solid- and liquid-state NMR further elaborated the structural alteration from the starting PHWE-xylan to the CNXs. First of all, the content

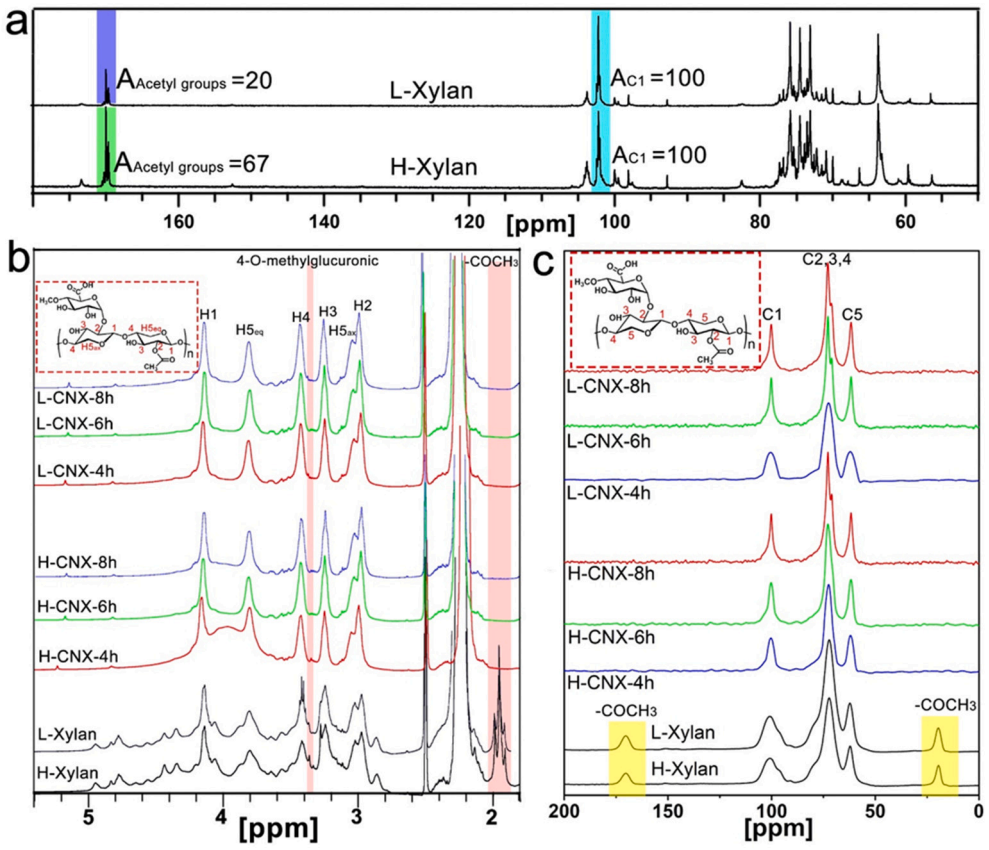

Fig. 2. (a) Quantitative ^{13}C NMR spectra of PHWE-xylan using DMSO-d_6 as solvent. (b) ^{1}H NMR spectra and (c) CP/MAS ^{13}C NMR spectra of PHWE-xylans and CNXs. Note: [P_{4444}][OAc]): DMSO-d_6 was used as the NMR solvent for (b) because that the crystalline CNXs are hardly dissolved in other general NMR solvents.

of acetyl groups in xylan was calculated by comparing the signal integration of acetyl groups (169.4–170.2 ppm) to anomeric carbons (C1, 101.5–102.8 ppm) as the ratio of $A_{Acetyl\ groups\ (170ppm)}/A_{C1(102ppm)}$, as displayed in Fig. 2a. The degree of substitution (*DS*) of the acetyl group was respectively 0.67 and 0.20 for H-xylan and L-xylan, which is in line with what was earlier reported (Kilpelainen et al., 2012). This suggests that the xylose units in the H-xylan fraction are more acetylated than those in the L-xylan fraction. This difference mainly accounts for their fractionation match to the cut-off size used in the ultrafiltration. As displayed in Fig. 2b, the proton signals at 4.1, 2.9, 3.2, 3.4, 3.8, and 3.1 ppm are corresponded to H1, H2, H3, H4, H5ax, and H5eq in xylan (Cao, Sun, Peng, Zhong, & Sun, 2013). The small signal at 3.4 ppm can be assigned to the 4-*O*-methylglucuronic units in xylan (H. Y. Yang, Song, Yuan, Xu, & Sun, 2011), which became almost undetectable in CNX after the alkali-catalyzed hydrolytic cleavage. In the solid-state cross-polarization magic angle spinning (CP/MAS) ^{13}C NMR spectra of xylans (Fig. 2c), 100.7, 72.4, and 61.9 ppm are assigned to C1, an overlapped contribution of C2/C3/C4, and C5, respectively (Meng et al., 2021; Teleman, Larsson, & Iversen, 2001). The overlapped contributions of C2/C3/C4 in H-CNXs and L-CNXs showed two split peaks at 72.8 and 71.1 ppm, especially for H-CNX-8 h, L-CNX-6 h, and L-CNX-8 h, which is indicative that two asymmetric xylose residues make up a crystallographic unit cell (Meng et al., 2021). This suggests that the as-synthesized nanoxylans might be in crystalline form. In addition, signals of acetyl groups that were originally present in the starting H-xylan and L-xylan at 170 and 20 ppm disappeared in the CNX samples, which again confirms the deacetylation effect of the alkali (Fig. 2c) (C. N. Yang et al., 2014). Moreover, in the liquid state ^{13}C NMR spectra, the dominating five signals at 103.1, 73.9, 75.1, 75.8, and 64.2 ppm can be assigned to the C1, C2, C3, C4, and C5 of xylan, respectively (Fig. S3) (Fundador, Enomoto-Rogers, Takemura, & Iwata, 2012). Some minor signals at 99.3, 72.1, and 59.8 ppm corresponding to C1, C5, and -OCH_3 of the 4-*O*-methylglucuronic units were observed for the PHWE-xylans, but were hardly detectable in the obtained CNXs after debranching synthesis (Peng, Peng, Bian, Xu, & Sun, 2011; H. Y. Yang et al., 2011). These NMR results strongly corroborate the success of alkali-catalyzed hydrolysis on removal of the side substitutions in PHWE-xylans.

3.2. Synthesis of hierarchical nano-assemblies of xylan: nanocluster hydrocolloids and submicron spheroids by EISA

The white-turbid colloidal suspension of the CNXs remained homogenous over a shelf time of 3 months (Fig. 3a), demonstrating their excellent aqueous dispersibility. For both the H-xylan and L-xylan series, the yield of CNX obtained in this alkali-catalytic hydrolysis gradually increased with the increase of reaction time from 4 h to 8 h (Fig. 3b). When the debranching was completed by 8 h, a yield around 40 % was confirmed for the CNX production. The hydrodynamic diameter measured by dynamic light scattering (DLS) for the CNXs was in the range of 160–200 nm and the zeta potential was registered in the range from −20 to −24 mV (Fig. 3c). In order to enhance the contrast of the CNX morphology, negative staining with uranyl acetate was applied in

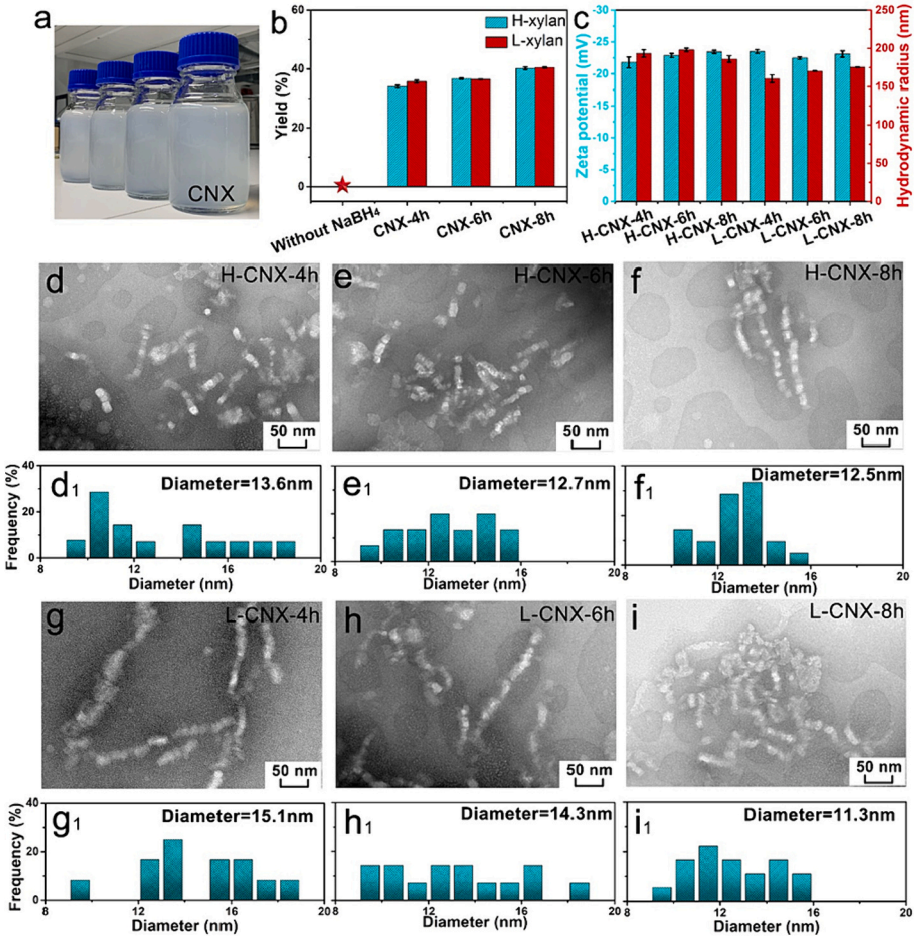

Fig. 3. (a) Photographs of scalable nanocluster hydrocolloids of nanoxylan (H-CNX-8 h). (b) Yield of CNX prepared with and without (star-shape) the reducing-end reformation. (c) Hydrodynamic radius and zeta potential of the as-prepared CNXs. TEM images of the head-to-toe assembly and diameter distribution of the primary nanoparticle in the hydrocolloids of CNXs (d and d_1, H-CNX-4 h; e and e_1, H-CNX-6 h; f and f_1 H-CNX-8 h; g and g_1, L-CNX-4 h; h and h_1, L-CNX-6 h; i and i_1, L-CNX-8 h).

TEM imaging. The morphology of CNX in all samples was imaged as worm-like nanocluster hydrocolloids self-assembled by primary crystallites (Fig. 3d–i). Interestingly, the nanocluster hydrocolloids present as an assembly of several primary crystallites connected from head to toe. This might explain the larger hydrodynamic radius of CNXs measured by DLS than the nano-dimensions as imaged in TEM. Importantly, a rather uniform size distribution in the range of 10–15 nm was confirmed for the primary crystallites obtained in the preparation of H-CNX-8 h and L-CNX-8 h (Fig. 3f_1–i_1). Similar morphology has earlier been reported for the xylan crystallites derived from the *Arabidopsis* mutant without sidechains, which is measured as 46 nm by 27 nm in hydrocolloids. It is also worth noting that these nanoxylans derived from xylans without sidechains tend to have a smaller dimension than other ones manufactured top-down by an oxidative method with either ammonium persulfate (30–50 nm) or alkaline periodate (30–80 nm) using the alkaline-extracted side-stream xylan as the starting material (Hao et al., 2022; H. R. Wang et al., 2023). We speculate that the elimination of side units supports the building-up of small dimensions in the CNXs via bottom-up self-assembly, as the growth of the nanoobject is spontaneously driven by molecular interactions.

A general definition of self-assembly is the spontaneous organization of materials through noncovalent interactions without external intervention, such as H-bond, *van der Waals* attraction, electrostatic forces, or π- π interactions. Fig. 4a presents the morphology of the CNXs prepared by EISA using nanocluster hydrocolloids at different substrate surfaces. For the two substrates used in the EISA, the silicon wafer with a water contact angle of 140.0 ± 1.1° is hydrophobic, and the glass plate with a water contact angle of 10.0 ± 1.1° is hydrophilic (Mu et al., 2010; Zhu, Tian, Liu, & Yang, 2019). However, the morphology of the CNXs prepared by EISA on these two substrate surfaces exhibited similarly circular structures with diameters ranging from 300 to 500 nm (Figs. 4b and S4). This phenomenon further confirmed the existence of *van der Waals* attraction and H-bonds during the evaporation process, leading to the formation of submicron particles in similar dimensions in the x and y directions. Furthermore, the polarized light microscope was used to observe the time-dependent morphology of CNX-spheroid prepared by EISA (Fig. S5). With the increase of drying time, nanocluster hydrocolloids are hierarchically assembled. Furthermore, AFM was used to investigate the three-dimensional morphology, height profile, and elastic modulus (DMT modulus) of the air-dried CNXs. Particles of CNX were again seen in the morphological analysis by AFM (Fig. 4c). In comparison with the SEM data, the particle size was slightly larger for both the H-CNX-8 h and the L-CNX-8 h. For instance, particles with a lateral diameter of 500–800 nm were observed for the self-assembled L-CNX-8 h obtained with EISA (Fig. 4c). The height of both types of CNX particles measured by AFM was in the range of 200–350 nm (see height profile in Fig. S6), which shows that the air-dried particles are not fully spherical, but rather spheroids with an oblate symmetry with a width: height aspect ratio around 2:1. The height of L-CNX was larger than that of H-CNX, indicating that L-CNX favors forming particles with a smaller aspect ratio under the same evaporation driving force, compared to H-CNX.

In addition, the average elastic modulus of L-CNX was higher than that of H-CNX, being 83 GPa (mode 30 GPa) compared to 47 GPa for H-CNX (mode 24 GPa). The difference between average value and mode values comes from the tailed distribution. Especially for L-CNX, an increased proportion of measurement points has an elastic modulus in the range of 100–225 GPa, (Fig. 4d, see corresponding stiffness modulus images in Fig. S7). These values are in the same order of magnitude as reported for cellulose nanocrystals (58–270 GPa, measured as the transverse elastic modulus with AFM) and chitin nanofibrils (40–60 GPa measured with tensile stress experiments) (Lahiji et al., 2010; Torres-

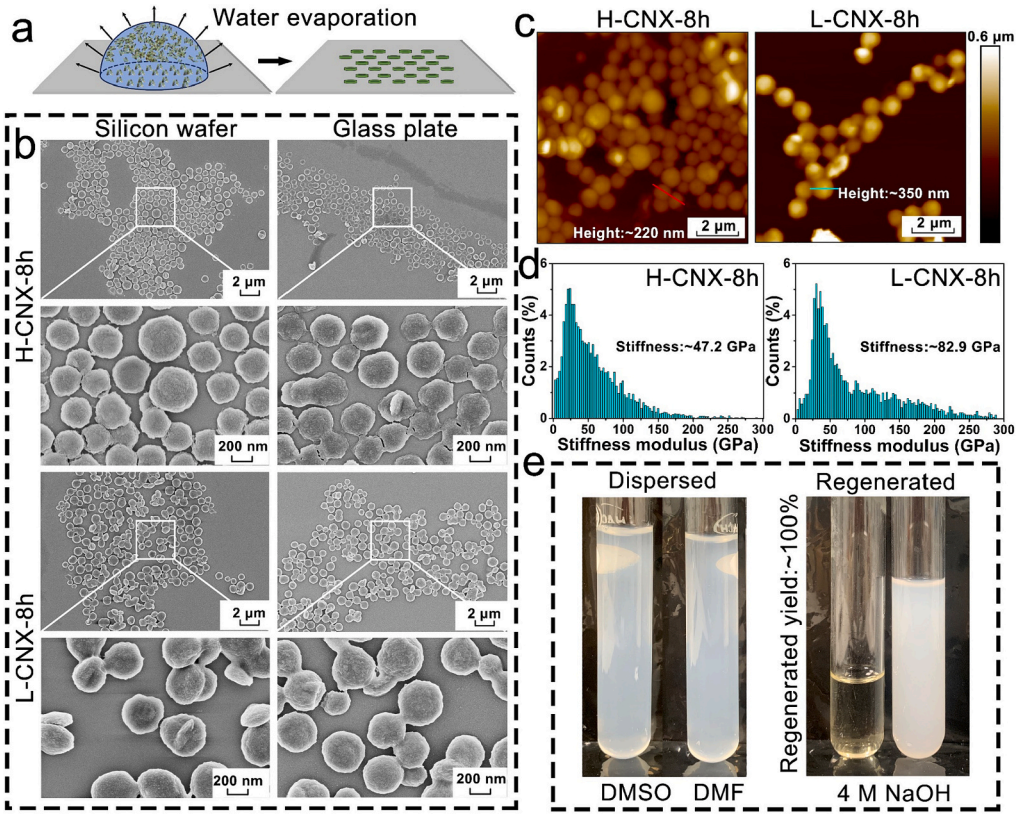

Fig. 4. (a) Schematic diagram of self-assembled CNX prepared by *EISA* at room temperature. (b) SEM images of the CNX-spheroid obtained by self-assembly on the substrate with different surface wettability (hydrophobic silicon wafer and hydrophilic glass plate). (c) Representative AFM height images of the CNX-spheroids and height values corresponding to the regions marked with lines in the AFM images. (d) Histograms of CNX-spheroids stiffness modulus distribution. (e) Photographs illustrating the dispersibility and solubility of CNX-spheroids investigated by dispersing/dissolving in DMSO, DMF, and 4 M NaOH.

Rendon, Schacher, Ifuku, & Walther, 2014). Therefore, the CNX reconstructed from debranched xylan through bottom-up self-assembly is anticipated to have a similar molecular stacking and arrangement analogous to the high-crystalline nanocellulose or nanochitin. It is also suggested that L-CNX may more strongly favor tight and tough molecular stacking in the molecular assembly, possibly attributed to the short and narrow-distributed dimension in the starting L-xylan than in the H-xylan.

Upon complete removal of the side substitutions, the molecular association in the reconstructed xylan is resistant to solvation, and therefore the CNX displays as a nanocluster hydrocolloid. Upon drying from the hydrocolloids, the primary xylan nanoparticles further self-assemble as unidirectional micro-sized particulates. Dried CNX is found insoluble in the polar organic solvent of DMSO or dimethyl formamide (DMF) but can form white-turbid hydrocolloids in a durable dispersibility. DMSO and DMF both have water-like H-bond ability, and hence they show a good dispersity to the nanoxylan materials (Fig. 4e). In alkali, CNX becomes soluble in 4 M NaOH at room temperature (Fig. 4e). Then, the nanocluster hydrocolloids of CNX can be regenerated by pH-shifting nanoprecipitation method. Thanks to the reformation of the reducing-end groups, no further peeling reaction occurs in this condition and the yield of CNX regeneration is close to 100 % (Fig. 4e). Furthermore, the morphology of regenerated CNX after pH-shifting nanoprecipitation was measured to investigate the regeneration effect, as shown in Fig. S8. The regenerated CNX presented similar morphology and diameter (10–15 nm) compared with the pristine CNX. This facile conversion from dry solid of CNX back to nanocluster hydrocolloids highlights a highly feasible workflow to store and transport the CNX in dry solids form as well as to regenerate the bio-based hydrocolloids on site in downstream applications.

3.3. Correlating macromolecular structure in the PHWE-xylan fraction with structural order of the self-assembled nanoxylan

XRD has confirmed that the PHWE-xylans and the freeze-dried CNXs are amorphous, whereas the air-dried CNXs present typical xylan hydrate crystals (Fig. 5a). The crystallinity (*CrI*) of CNXs was correlated with the degree of debranching and the humidity during the formation, which is important in achieving a higher *CrI* (Hao et al., 2022; Horio & Imamura, 1964; Zhang et al., 2023). Specifically, the relative *CrI* of H-CNX-4 h, H-CNX-6 h, H-CNX-8 h, L-CNX-4 h, L-CNX-6 h, and L-CNX-8 h was 37.9 %, 38.8 %, 38.7 %, 40.5 %, 40 %, and 41 %, respectively (Fig. 5b). The L-xylan-derived CNXs have a higher crystallinity than the ones derived from H-xylan. In addition, the *CrI* of the CNX is closely correlated with the degree of debranching: a higher degree of debranching, a higher degree of crystallinity. The highest crystallinity was reached when the removal of side substitutions was completed at a reaction duration of 8 h, and sufficient water molecules could be in

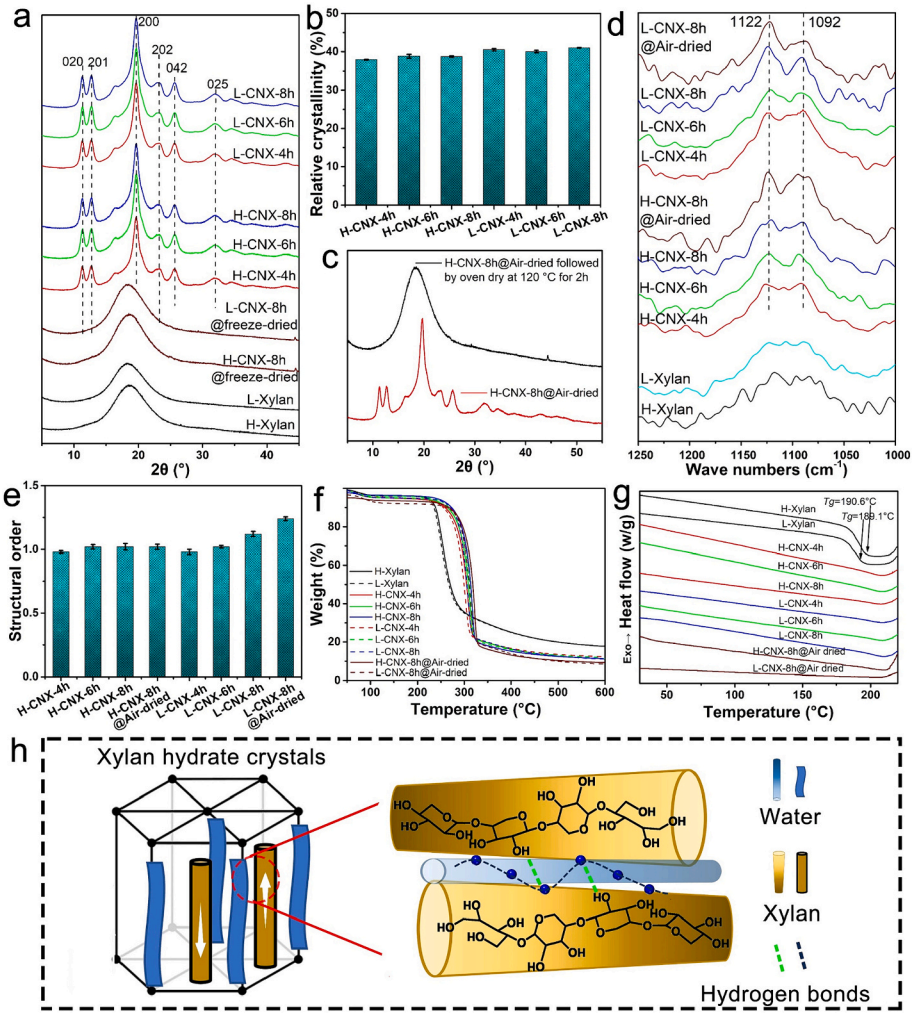

Fig. 5. (a) XRD patterns and (b) the corresponding relative *CrI* values of xylan, air-dried CNX, and freeze-dried CNX. (c) XRD patterns of air-dried CNX and air-dried CNX followed by oven drying at 120 °C for 2 h. (d) Raman spectra, (e) Structure order, (f) TG, and (g) DSC curves of xylan, air-dried CNX, and freeze-dried CNX. (h) Schematic illustration of the molecular packing in xylan hydrate crystals and the connecting H-bonds.

contact during the nanoprecipitation and air-drying of CNX. Furthermore, the polarized light microscope was used to investigate the crystal structure of the CNX-spheroid prepared by EISA, and the image is displayed in Fig. S9. As expected, the CNXs with higher crystallinity present color manifestation, owing to the anisotropic properties provided by oriented structure through long-chain molecular interaction. Moreover, as shown in Fig. S10, the regenerated CNX exhibited similar crystal structure compared with the pristine CNX. However, the crystallinity of CNX is sensitive to the relative humidity. As shown in Fig. 5a and c, the crystallization peaks of CNX disappeared completely after lyophilization or oven drying at 120 °C. At this time, the hydrated xylan crystals were destructed as the physically absorbed water molecules were ablated.

In Raman spectra (Fig. 5d), the peaks at 1122 and 1092 cm^{-1} belong to the C—O stretch, which is attributed to glycosidic link and ring vibrations of xylan (Kacurakova et al., 1999; Shen, Zhong, & Hu, 2004). Moreover, the peak in the range of 2988 cm^{-1} can be ascribed to acetyl groups of xylan (Fig. S11), and the multi-peak area located at about 1200–1500 cm^{-1} can be assigned to the acetyl and methyl-glucuronate groups (Farghal, Nebsen, & El-Sayed, 2023). The broad C—H stretching feature at 2940 cm^{-1} in xylan shifts to 2896 cm^{-1} in CNX, which is probably due to the enhanced intra- and inter-chain hydrogen bonding (Fig. S11) (Jahn, Schroder, Futing, Schenzel, & Diepenbrock, 2002; Kolpak & Blackwell, 1976). As the structure of linear xylan polymer is considered in similar analog with cellulose, we tried to use the I^{1122}/I^{1092} ratio to assess the structural order (*SO*) of crystallized nanoxylans. The I^{1122}/I^{1092} ratio has been used to calculate the *SO* of cellulose (Fig. S12) (Alves et al., 2016). The I^{1122}/I^{1092} ratio of H-CNX-4 h, H-CNX-6 h, H-CNX-8 h, H-CNX-8 h@Air-dried, L-CNX-4 h, L-CNX-6 h, L-CNX-8 h, and L-CNX-8 h@Air-dried were 0.98, 1.02, 1.02, 1.02, 0.98, 1.02, 1.12, and 1.24, respectively (Fig. 5e), which again corroborates the increased intra- and inter-chain hydrogen bonding formed upon the complete removal of side substitutions. Short and narrow-distributed polymer chains in L-CNXs may decrease their degree of freedom, which consequently increases the regularity in the arrangement of the xylan polymer chains. Both the *CrI* and *SO* of the L-xylan-derived CNX were higher than those of the H-xylan-derived CNX. This suggests that the chain length and homogeneity of debranched PHWE-xylan dictate the *SO* of the CNX as received from the bottom-up building of the nanocrystals.

The xylan and CNX samples were analyzed by DSC and TGA, in order to delineate key thermal parameters, such as glass transition temperature (*Tg*) and decomposition temperature. As shown in the TG curves (Fig. 5f), the initial decomposition temperature (onset temperature, T_o) and the temperature at maximum degradation rate (peak temperature, T_{max}) of the H-xylan were 233.6 and 250 °C, respectively. As evident, the T_o and T_{max} of H-CNXs and L-CNXs were much higher than those of xylan. This phenomenon is associated with the crystallinity in the CNXs. The *Tg* of H-xylan and L-xylan was 190.6 °C and 189.1 °C, respectively, as shown in the DSC curves (Fig. 5g). *Tg* is the typical temperature of an amorphous polymer, at which increased molecular mobility results in significant changes in the thermal properties, while high crystallinity restricts the mobility of polymer chains, and eventually elevates the *Tg* (Sorolla-Rosario, Llorca-Porcel, Perez-Martinez, Lozano-Castello, & Bueno-Lopez, 2022; Xie et al., 2020; Zuza et al., 2008). Thus, as displayed in Fig. 5g, the *Tg* of CNX was hardly detectable, corroborating the increase in the *CrI* and the strong H-bond network in the CNX. Finally, Fig. 5h presents a possible schematic illustration of the molecular packing in xylan hydrate crystals. Xylan hydrate that is crystallized from the aqueous system was reported with a 3-fold (one turn per three glycosidic bonds) helical structure, which is considered as the most stable conformation in xylan hydrate crystals (Chanzy, Dube, & Marchessault, 1979; Nieduszynski & Marchessault, 1972). During nanoprecipitation and air drying, the xylan chain would be aligned along the polymer chain direction and could be packed in an antiparallel manner in the unit cell of xylan hydrate crystal, similar to the formation of cellulose II during mercerization. In this manner, highly uniform CNX is bottom up yielded via the molecular self-assembly of linear xylan polymer, driven by the hydrogen bonds between hydroxyl groups and water molecular, eventually forming a 3-fold helix in xylan hydrate crystals (Fig. 5h). Compared with other nanostructured polycrystalline polysaccharides such as cellulose nanocrystals and chitin nanocrystals to inherit the toughness and resistance when they are produced top down, the as-reported CNX builds in crystallinity and chemical resistance during the self-assembly process of nanosynthesis (Elazzouzi-Hafraoui et al., 2008; Goodrich & Winter, 2007).

3.4. Ultralong phosphorescence emission dependent on the structural order of nanoxylan

Strategically, we extend the correlation of macromolecular structure in the PHWE-xylan fraction to the phosphorescence-emission of nanoxylan, as it is a microscale physical property that is closely associated with the molecular conformation and stacking in xylan (Shi et al., 2023; Xu, Chen, Zheng, & Huang, 2016). Ultralong phosphorescence refers to an optical phenomenon in which the light emitting sustains for >100 ms after removing the excitation source (Xu et al., 2016). Several reports have established that xylan emits color-tunable and long-lived phosphorescence, owing to the heterogeneous emissive oxygen clusters (Gong et al., 2013; Lu et al., 2022). Commonly, to stimulate a long phosphorescence one can aim (i) to enhance the intersystem crossing and spin-orbit coupling to populate triplet excitons, and (ii) to construct a rigid crystalline environment and tight cluster by clustering reconstruction in order to suppress non-radiative decay of long phosphorescence (Gao et al., 2023; Lu et al., 2022). For instance, 2,3-dialdehyde cellulose facilitates the reconstruction of a more rigid crystalline environment, which protects the triplet excitons from quenching and decay (Gao et al., 2023). Moreover, tunable ultralong phosphorescence was achieved by fixing various clusters of oxygen groups of xylan in a rigid environment provided by high crystallization, as reported by Lv et al. (Lu et al., 2022). For the bottom-up synthesis of CNX, the complete debranching of xylan is hypothesized to favor internal clusterization and a rigid environment as resulted by intra- and inter-chain H bonds, which would contribute to suppressing the decay of phosphorescence.

The photophysical properties of CNX were measured, as displayed in Fig. 6a. When excited at 300 nm with a continuous-wave Xe lamp, the PHWE-xylans and CNXs exhibit two luminescence emission peaks at 350–420 nm (peaking in UV/blue) and 450–600 nm (peaking in green), respectively. The UV/blue peak is short-lived, as it cannot be observed after a 0.2 ms delay, but the green emission is longer-lived (Fig. S13). It is to be noted that this 0.2 ms is not the actual limit for the UV/blue emission lifetime but it is the shortest delay available with the used measurement setup. The afterglow duration of phosphorescence of the CNXs was quantified in Fig. 6b based on fading until the 0.32 mcd/m^2 luminance set as the limit for visibility of a standard human eye in DIN 76510–1 (Norm, 2009). What's more, the capture of afterglow was carried out with a video camera, as illustrated in Fig. 6c. The luminescence color under the UV lamp is white or blueish white for all samples due to the simultaneously emitting UV/blue and green bands. When the lamp is turned off, the emission is green. After 2 min exposure of 302 nm, the afterglow fading measured for the PHWE-xylans and freezing-dried CNXs was weaker than that was measured for the air-dried crystalline CNXs. The debranched xylan is proven with better phosphorescence emitting than its starting PHWE-xylan, attributed to the crowded macromolecular architecture as reconstructed in the CNX driven by *van der* Waals forces and H-bonds. With the increase of the debranching degree, an increase in the afterglow duration of the CNX was detected (Fig. 6b and c) with the longest extending to 12 s. It is conceivable that higher degree of side-substitution removal contributes to higher steric hindrance, thereby suppressing the duration of afterglow. For the linear xylan of H-CNX-8 h and the L-CNX-8 h, the freeze-dried samples showed a decrease in the duration of afterglow, compared with their air-dried counterparts, which again confirms that the rigid crystalline

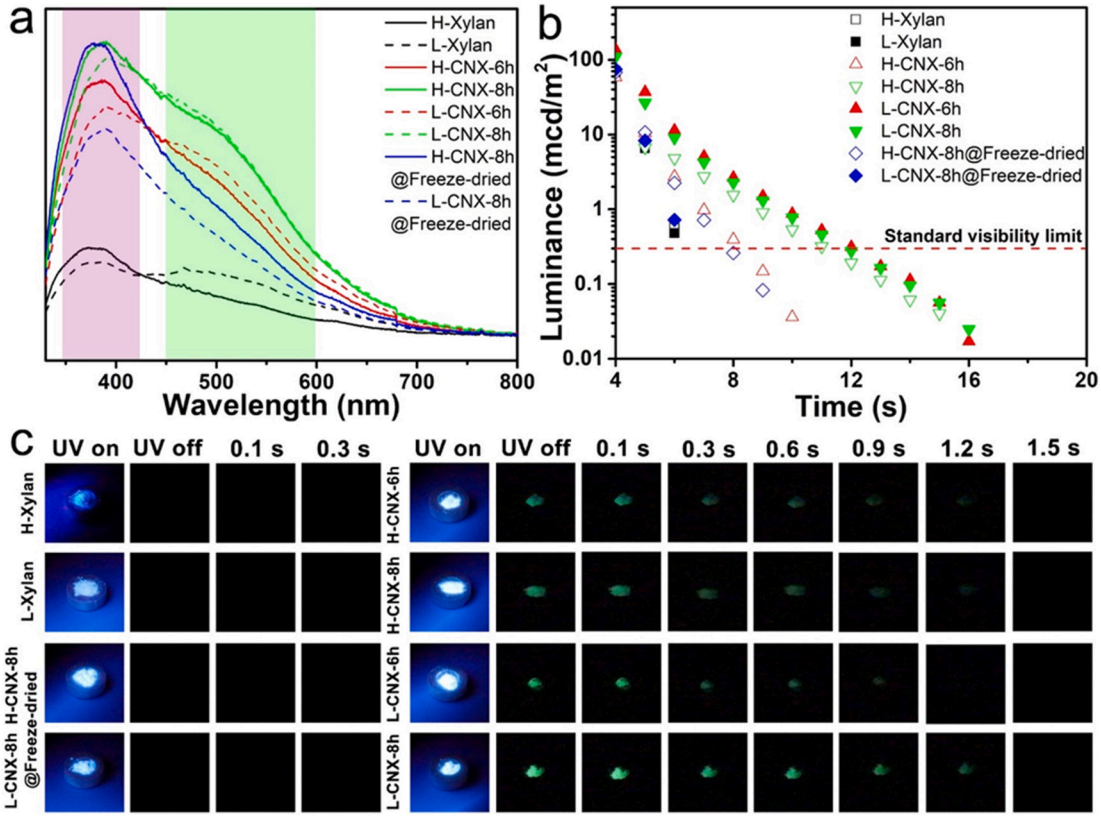

Fig. 6. (a) Emission spectrum of the PHWE-xylans and CNXs excited at 300 nm with a delay time of 1 ms. (b) Afterglow fading curves of the PHWE-xylans and CNXs measured after 2 min exposure of 302 nm. (c) Photographs of the long-lived phosphorescence emission of the CNXs after turning off UV excitations (302 nm) under ambient conditions.

environment in the xylan hydrate crystal can suppress the decay of phosphorescence (Fig. 6b). Between the xylan hydrate crystal of air-dried H-CNX-8 h and L-CNX-8 h, the L-CNX was confirmed with a longer afterglow duration. The higher *SO* in L-CNX promoted long-lived emission because the rigid environment constructed by intra- and inter-molecule interactions could restrict the aggregated clusters and molecular motions, and thus suppress the non-radiative relaxation of long phosphorescence (Fig. S14). Among the sample groups, the specimen of air-dried L-CNX-8 h exhibited the longest afterglow duration and its afterglow phosphorescence could be observed with our camera setup for 1.5 s (Fig. 6c). This performance is in line with what was earlier reported by Lv et al. for the lifetime of ultralong organic phosphorescence emitted by the low-branched alkaline-extracted xylan (Lu et al., 2022). However, under standard measurement conditions (DIN 67510–1), the materials studied here show afterglow that is visible to the naked eye for >10 s.

3.5. *Efficiency of this bottom-up approach in converting amorphous biorefinery xylan to hierarchical crystalline nanomaterials*

The present research has showcased a synthesis that converts the amorphous xylan preserved in biomass to hierarchical crystalline nano-

Table 2
Comparison of approaches and synthesis conditions for manufacturing crystalline nanomaterial of xylan recently published in the literature.

Starting material	Preparation method	Reaction condition	Nanoxylan yield (wt%)	Nanoxylan dimension	Nanoxylan shape	Ref.
Alkaline-extracted side-stream xylan	Ammonium persulfate oxidation and subsequent ultrasonication	60 °C and 12 h	4–9	30–50 nm	Platelet	(Wang et al., 2023)
Alkaline-extracted side-stream xylan	Alkaline periodate oxidation and subsequent ultrasonication	25 °C and 72 h	4–9	30–80 nm	Platelet	(Hao et al., 2022)
Alkaline-extracted side-stream xylan	Dissolved in tetraethylammonium hydroxide and regenerated by adding water	50 °C and 15 h	12–18	60–70 nm	Platelet	(Liu et al., 2023)
Alkaline- extracted wood xylan	Dispersed in DMSO and heat-induced crystallization	60 °C and 2–20 days	20–30	200–850 nm	Rod-like	(Meng et al., 2021)
Alkaline- extracted *esparto* xylan	Self-assembly and recrystallization from supersaturated solutions	121 °C and 3 h	20–30	400 nm – 2.5 μm	Hexagonal convex platelet	(Zhang et al., 2023)
Alkaline- extracted xylan from *Arabidopsis* mutant	Self-assembly and recrystallization from supersaturated solutions	121 °C and 4 h	20–30	~40 nm crystallite	Nanocluster hydrocolloids and spherulitic superstructure up to 5 μm	(Johnson, Mottiar, et al., 2023)
Water-soluble PHWE-birch xylan	One-pot debranching and deacetylation to xylan, pH-neutralization, and subsequent EISA	150 °C and 8 h	28	10–15 nm crystallite	Nanocluster hydrocolloids and submicron spheroids	This work

Note: the yield of nanoxylan was calculated based on the content of hemicellulose xylan in biomass.

assemblies. In Table 2, we compare our approach to fabricate the CNX with other existing approaches in the literature and discuss their distinctions on such perspectives as the starting material, preparation method, yield of nanoxylan, reaction temperature, and the dimension of nanoxylan. In comparison with other manufacturing associated with the alkaline-extracted side-stream xylan where the conversion efficiency is compromised by the unavoidable main-chain peeling, current bottom-up nanosynthesis using biorefinery xylan produces CNX in a higher yield. Meanwhile, using the water-soluble PHWE-xylan as a starting material, a controllable macromolecular characteristic is accessible in the process to yield the linear xylan polymer. We succeeded to correlate the molecular structure in the starting xylan-fraction with the ordered structure in the macromolecular assembly of debranched xylan, and further with the physical property of phosphorescence emitting of nanoxylan. Overall, self-assembled nanomaterials of crystalline xylan as stable hydrocolloids undoubtedly increase the accessibility to nano-sized xylan and open new routes gauge for this class of bio-based building block in constructing functional thin coatings or monolithic materials in unprecedented high value-added applications as foreseen.

4. Conclusion

In summary, we adopt a bottom-up strategy to convert water-soluble and amorphous xylan obtained in a PHWE-biorefinery to nanoxylan as stable hydrocolloids. The reformation of the end-group by borohydride reduction to a primary alcohol effectively prevents the main-chain peeling when the substitutions of side-sugar units and acetyl groups are cleaved at an elevated temperature under alkaline conditions. This eventually tailor makes the branched PHWE-xylans as almost linear biopolymer composed of >90 wt% xylose units. Multi-instrumental analysis (composition analysis and NMR) confirmed the almost complete removal of side substitutions. Driven by the intra- and inter-molecular interactions, i.e., *van der Waals* attraction and H-bond, the debranched xylan self-assembles as primary crystallites in uniform diameter of 10–15 nm, which are spontaneously assembled head to toe as worm-like nanoclusters in the hydrocolloids. EISA yields submicron spheroids that are hierarchically assembled with primary nanoparticles of CNX, exhibiting a high average material elastic modulus of 47–83 GPa (mode 24–30 GPa) for this type of crystalline biopolymer. L-CNXs present a higher structure order and crystallinity, as short and narrow-distributed polymer chains may favor a tight and ordered molecular stacking in the molecular assembly. This structure-performance correlation was confirmed for the phosphorescence-emission of nanoxylans: the L-CNX made of short and narrow-distributed xylan chains promotes long-lived phosphorescence than the H-CNX, attributed to the rigid clusterization and high crystallinity within this nanoxylan type.

CRediT authorship contribution statement

Yidong Zhang: Writing – original draft, Visualization, Validation, Methodology, Investigation, Formal analysis, Data curation. **Luyao Wang:** Writing – original draft, Methodology, Data curation. **Hao Zhang:** Writing – review & editing, Validation, Data curation. **Emil Rosqvist:** Writing – review & editing, Investigation, Formal analysis, Data curation. **Mika Lastusaari:** Writing – review & editing, Validation, Methodology, Formal analysis, Data curation. **Jouko Peltonen:** Writing – review & editing, Validation, Resources. **Lari Vähäsalo:** Resources. **Chunlin Xu:** Writing – review & editing, Supervision, Resources, Investigation, Funding acquisition. **Xiaoju Wang:** Writing – review & editing, Writing – original draft, Validation, Supervision, Project administration, Methodology, Investigation, Conceptualization. **Andrey Pranovich:** Writing – review & editing, Writing – original draft, Validation, Supervision, Methodology, Investigation, Data curation, Conceptualization.

Declaration of competing interest

The authors declare that they have no known competing financial interests or personal relationships that could have appeared to influence the work reported in this paper.

Data availability

Data will be made available on request.

Acknowledgements

Y. Zhang would like to acknowledge the financial support from the China Scholarship Council (NO. 202207960008). L. Wang and C. Xu would like to acknowledge funding from Business Finland Project (43674/31/2020). X. Wang would like to thank Academy of Finland (333158) for the Research Fellow Funds for her research at ÅAU. E. Rosqvist and J. Peltonen acknowledge funding from Jane and Aatos Erkko Foundation (Project: Anti-bacterial channeling from waste to human health). Electron microscopy samples were processed and analyzed in the Electron Microscopy Laboratory, Institute of Biomedicine, University of Turku, which receives financial support from Biocenter Finland. Parts of the research used the Research Council of Finland Infrastructure 'Printed Intelligence Infrastructure' (PII-FIRI).

Appendix A. Supplementary data

Detailed characterization methods; xylan suspension with (Fig. S1) and without (Fig. S2) $NaBH_4$ reduction to reform the reducing-ends before and after neutralization; ^{13}C NMR spectra of PHWE-xylans and CNXs (Fig. S3); SEM images of CNX obtained by EISA (Fig. S4); time-dependent profile of CNX spheroid prepared by EISA (Fig. S5); the height profile (Fig. S6), stiffness of CNX-spheroids (Fig. S7); TEM images of regenerated CNX (Fig. S8); the polarized light microscope of CNX-spheroids (Fig. S9); XRD patterns of regenerated CNX (Fig. S10); Raman spectra of the PHWE-xylans, CNXs (Fig. S11), and cellulose powder (Fig. S12); phosphorescence emission spectrum of H-CNX-6 h measured after a 0.2 ms delay after an excitation pulse at 300 nm (Fig. S13); Jablonski diagram of possible phosphorescence mechanism of CNX (Fig. S14); TG data of the PHWE-xylans and CNXs (Table S1). Supplementary data to this article can be found online at https://doi.org/10.1016/j.carbpol.2024.122089.

References

Aliev, A. E., Oh, J. Y., Kozlov, M. E., Kuznetsov, A. A., Fang, S. L., Fonseca, A. F., … Baughman, R. H. (2009). Giant-stroke, superelastic carbon nanotube aerogel muscles. *Science, 323*(5921), 1575–1578. https://doi.org/10.1126/science.1168312

Alves, A. P. P., de Oliveira, L. P. Z., Castro, A. A. N., Neumann, R., de Oliveira, L. P. C., Edwards, H. G. M., & Sant'Ana, A. C. (2016). The structure of different cellulosic fibres characterized by Raman spectroscopy. *Vibrational Spectroscopy, 86*, 324–330. https://doi.org/10.1016/j.vibspec.2016.08.007

Andrewartha, K. A., Phillips, D. R., & Stone, B. A. (1979). Solution properties of wheat-flour arabinoxylans and enzymically modified arabinoxylans. *Carbohydrate Research, 77*(DEC), 191–204. https://doi.org/10.1016/s0008-6215(00)83805-7

Bai, L., Liu, L., Esquivel, M., Tardy, B. L., Huan, S. Q., Niu, X., … Rojas, O. J. (2022). Nanochitin: Chemistry, structure, assembly, and applications. *Chemical Reviews*. https://doi.org/10.1021/acs.chemrev.2c00125

Benouadah, N., Pranovich, A., Aliouche, D., Labidi, J., & Willfor, S. (2021). Optimization of the extraction of galactoglucomannans from Pinus halepensis. *Holzforschung, 75*(6), 563–573. https://doi.org/10.1515/hf-2020-0095

Bosmans, T. J., Stepan, A. M., Toriz, G., Renneckar, S., Karabulut, E., Wagberg, L., & Gatenholm, P. (2014). Assembly of debranched xylan from solution and on nanocellulosic surfaces. *Biomacromolecules, 15*(3), 924–930. https://doi.org/10.1021/bm4017868

Cao, X. F., Sun, S. N., Peng, X. W., Zhong, L. X., & Sun, R. C. (2013). Synthesis and characterization of cyanoethyl hemicelluloses and their hydrated products. *Cellulose, 20*(1), 291–301. https://doi.org/10.1007/s10570-012-9814-1

Chanda, S. K., Hirst, E. L., Jones, J. K. N., & Percival, E. G. V. (1950). The constitution of xylan from esparto grass (Stipa-tenacissima, L). *Journal of the Chemical Society*, (May), 1289–1297. https://doi.org/10.1039/jr9500001289

Chanzy, H., Dube, M., & Marchessault, R. H. (1979). Structural polymorphism of (1–4)-beta-d-xylan. Polymer, 20(8), 1037–1039, doi:https://doi.org/10.1016/0032-3861(79)90205-2.

Cheng, S. Y., Zhang, C., Li, J. J., Pan, X. H., Zhai, X. R., Jiao, Y. Z., … Qi, X. L. (2021). Highly efficient removal of antibiotic from biomedical wastewater using Fenton-like catalyst magnetic pullulan hydrogels. *Carbohydrate Polymers, 262*. https://doi.org/10.1016/j.carbpol.2021.117951

Ebringerova, A., & Heinze, T. (2000). Xylan and xylan derivatives - Biopolymers with valuable properties, 1 - Naturally occurring xylans structures, procedures and properties. Macromolecular Rapid Communications, 21(9), 542–556, Retrieved from <Go to ISI>://WOS:000087943400003.

Ebringerová, A., Hromádková, Z., & Heinze, T. (2005). Hemicellulose. In T. Heinze (Ed.), *Polysaccharides 1: Structure, characterization and use* (pp. 1–67).

Elazzouzi-Hafraoui, S., Nishiyama, Y., Putaux, J. L., Heux, L., Dubreuil, F., & Rochas, C. (2008). The shape and size distribution of crystalline nanoparticles prepared by acid hydrolysis of native cellulose. *Biomacromolecules, 9*(1), 57–65. https://doi.org/10.1021/bm700769p

Farghal, H. H., Nebsen, M., & El-Sayed, M. M. H. (2023). Multifunctional chitosan/xylan-coated magnetite nanoparticles for the simultaneous adsorption of the emerging contaminants Pb(II), salicylic acid, and Congo red dye. *Water, 15*(4). https://doi.org/10.3390/w15040829

Fry, S. C. (1988). *The growing plant cell wall: Chemical and metabolic analysis*. Longman Group Limited.

Fundador, N. G. V., Enomoto-Rogers, Y., Takemura, A., & Iwata, T. (2012). Syntheses and characterization of xylan esters. *Polymer, 53*(18), 3885–3893. https://doi.org/10.1016/j.polymer.2012.06.038

Gao, Q., Rao, J., Lv, Z. W., Shi, M. C., Chen, M. X., Chen, G. G., … Peng, F. (2023). Stereospecific redox-mediated clusterization reconstruction for constructing long-lived, color-tunable, and processable phosphorescence cellulose. *Chemical Engineering Journal, 451*. https://doi.org/10.1016/j.cej.2022.138923

Gellerstedt, G., & Li, J. B. (1996). An HPLC method for the quantitative determination of hexeneuronic acid groups in chemical pulps. Carbohydrate Research, 294, 41–51, Retrieved from <Go to ISI>://WOS:A1996VV08500004.

Ghasemlou, M., Daver, F., Ivanova, E. P., Habibi, Y., & Adhikari, B. (2021). Surface modifications of nanocellulose: From synthesis to high-performance nanocomposites. *Progress in Polymer Science, 119*. https://doi.org/10.1016/j.progpolymsci.2021.101418

Gomes, T. M. P., de Sousa, A. R. M., Belenkiy, Y. I., & Evtuguin, D. V. (2020). Xylan accessibility of bleached eucalypt pulp in alkaline solutions. *Holzforschung, 74*(2), 141–148. https://doi.org/10.1515/hf-2019-0023

Gong, Y. Y., Tan, Y. Q., Mei, J., Zhang, Y. R., Yuan, W. Z., Zhang, Y. M., … Tang, B. Z. (2013). Room temperature phosphorescence from natural products: Crystallization matters. *Science China: Chemistry, 56*(9), 1178–1182. https://doi.org/10.1007/s11426-013-4923-8

Goodrich, J. D., & Winter, W. T. (2007). Alpha-chitin nanocrystals prepared from shrimp shells and their specific surface area measurement. *Biomacromolecules, 8*(1), 252–257. https://doi.org/10.1021/bm0603589

Habibi, Y., Lucia, L. A., & Rojas, O. J. (2010). Cellulose nanocrystals: Chemistry, self-assembly, and applications. *Chemical Reviews, 110*(6), 3479–3500. https://doi.org/10.1021/cr900339w

Hao, X., Li, N., Wang, H. R., Jia, S. Y., Liu, Q. L., & Peng, F. (2021). Dialdehyde xylan-based sustainable, stable, and catalytic liquid metal nano-inks. *Green Chemistry, 23*(19), 7796–7804. https://doi.org/10.1039/d1gc02696h

Hao, X., Lv, Z. W., Wang, H. R., Rao, J., Liu, Q. L., Lu, B. Z., & Peng, F. (2022). Top-down production of sustainable and scalable hemicellulose nanocrystals. *Biomacromolecules, 23*(11), 4607–4616. https://doi.org/10.1021/acs.biomac.2c00841

Horio, M., & Imamura, R. (1964). Crystallographic study of xylan from wood. *Journal of Polymer Science Part A-General Papers, 2*(2PA), 627. https://doi.org/10.1002/pol.1964.100020206

Jahn, A., Schroder, M. W., Futing, M., Schenzel, K., & Diepenbrock, W. (2002). Characterization of alkali treated flax fibres by means of FT Raman spectroscopy and environmental scanning electron microscopy. *Spectrochimica Acta Part a-Molecular And Biomolecular Spectroscopy, 58*(10), 2271–2279. https://doi.org/10.1016/s1386-1425(01)00697-7

Johnson, A. M., Karaaslan, M. A., Cho, M., Ogawa, Y., & Renneckar, S. (2023). Exploring the impact of water on the morphology and crystallinity of xylan hydrate nanotiles. *Carbohydrate Polymers, 319*. https://doi.org/10.1016/j.carbpol.2023.121165

Johnson, A. M., Mottiar, Y., Ogawa, Y., Karaaslan, M. A., Zhang, H. Y., Hua, Q., … Renneckar, S. (2023). The formation of xylan hydrate crystals is affected by sidechain uronic acids but not by lignin. *Cellulose, 30*(13), 8475–8494. https://doi.org/10.1007/s10570-023-05422-2

Kacurakova, M., Wellner, N., Ebringerova, A., Hromadkova, Z., Wilson, R. H., & Belton, P. S. (1999). Characterisation of xylan-type polysaccharides and associated cell wall components by FT-IR and FT-Raman spectroscopies. *Food Hydrocolloids, 13*(1), 35–41. https://doi.org/10.1016/s0268-005x(98)00067-8

Kilpeläinen, P., Kitunen, V., Pranovich, A., Ilvesniemi, H., & Willför, S. (2013). Pressurized hot water flow-through extraction of birch sawdust with acetate pH buffer. Bioresources, 8(4), 5202–5218, Retrieved from <Go to ISI>://WOS:000328280700033.

Kilpelainen, P., Leppanen, K., Spetz, P., Kitunen, V., Ilvesniemi, H., Pranovich, A., & Willfor, S. (2012). Pressurised hot water extraction of acetylated xylan from birch sawdust. *Nordic Pulp & Paper Research Journal, 27*(4), 680–688. https://doi.org/10.3183/npprj-2012-27-04-p680-688

Kolpak, F. J., & Blackwell, J. (1976). Determination of structure of cellulose II. *Macromolecules, 9*(2), 273–278. https://doi.org/10.1021/ma60050a019

Lagerquist, L., Pranovich, A., Sumerskii, I., von Schoultz, S., Vähäsalo, L., Willför, S., & Eklund, P. (2019). Structural and thermal analysis of softwood lignins from a pressurized hot water extraction biorefinery process and modified derivatives. *Molecules, 24*(2). https://doi.org/10.3390/molecules24020335

Lahiji, R. R., Xu, X., Reifenberger, R., Raman, A., Rudie, A., & Moon, R. J. (2010). Atomic force microscopy characterization of cellulose nanocrystals. *Langmuir, 26*(6), 4480–4488. https://doi.org/10.1021/la903111j

Liu, Q. L., Tian, R., Lv, Z. W., Wu, Y. Y., Lv, B. Z., Hao, X., … Peng, F. (2023). Rapid, selective, and room temperature dissolution of crystalline xylan by a hydrotrope. *Carbohydrate Polymers, 300*. https://doi.org/10.1016/j.carbpol.2022.120245

Lu, B. Z., Gao, Q., Li, P. Y., Rao, J., Lv, Z. W., Shi, M. C., … Peng, F. (2022). Natural ultralong hemicelluloses phosphorescence. Cell Reports Physical. *Science, 3*(9). https://doi.org/10.1016/j.xcrp.2022.101015

Meng, Z. J., Sawada, D., Laine, C., Ogawa, Y., Virtanen, T., Nishiyama, Y., … Kontturi, E. (2021). Bottom-up construction of xylan nanocrystals in D methyl sulfoxide. *Biomacromolecules, 22*(2), 898–906. https://doi.org/10.1021/acs.biomac.0c01600

Mu, X. A., Liang, Q. L., Hu, P., Ren, K. N., Wang, Y. M., & Luo, G. A. (2010). Selectively modified microfluidic chip for solvent extraction of Radix salvia miltiorrhiza using three-phase laminar flow to provide double liquid-liquid interface area. *Microfluidics and Nanofluidics, 9*(2–3), 365–373. https://doi.org/10.1007/s10404-009-0554-y

Nieduszynski, I., & Marchessault, R. (1972). Structure of β, D (1–> 4')-xylan hydrate. *Biopolymers: Original Research on Biomolecules, 11*(7), 1335–1344.

Nishiyama, Y. (2018). Molecular interactions in nanocellulose assembly. Philosophical Transactions Of the Royal Society A-Mathematical Physical and. *Engineering Sciences, 376*(2112). https://doi.org/10.1098/rsta.2017.0047

Norm, D. (2009). *Phosphorescent pigments and products–Part 1: Measurement and marking at the producer*.

Peng, P., Peng, F., Bian, J., Xu, F., & Sun, R. C. (2011). Studies on the starch and hemicelluloses fractionated by graded ethanol precipitation from bamboo Phyllostachys bambusoides F. Shouzhu Yi. *Journal of Agricultural and Food Chemistry, 59*(6), 2680–2688. https://doi.org/10.1021/jf1045766

Pinto, P. C., Evtuguin, D. V., & Neto, C. P. (2005). Effect of structural features of wood biopolymers on hardwood pulping and bleaching performance. *Industrial & Engineering Chemistry Research, 44*(26), 9777–9784. https://doi.org/10.1021/ie050760o

Pranovich, A., Holmbom, B., & Willfor, S. (2016). Two-stage hot-water extraction of galactoglucomannans from spruce wood. *Journal of Wood Chemistry and Technology, 36*(2), 140–156. https://doi.org/10.1080/02773813.2015.1104543

Qi, X. L., Pan, W. H., Tong, X. Q., Gao, T., Xiang, Y. J., You, S. Y., … Shen, J. L. (2021). e-Polylysine-stabilized agarose/polydopamine hydrogel dressings with robust photothermal property for wound healing. *Carbohydrate Polymers, 264*. https://doi.org/10.1016/j.carbpol.2021.118046

Rao, J., Lv, Z. W., Chen, G. G., & Peng, F. (2023). Hemicellulose: Structure, chemical modification, and application. *Progress in Polymer Science, 140*. https://doi.org/10.1016/j.progpolymsci.2023.101675

Roubroeks, J. P., & Kondo, T. (2012). Nano- and microstructures in stretched and non-stretched blend gels of cellulose and hemicelluloses. *Holzforschung, 66*(8), 993–1000. https://doi.org/10.1515/hf-2011-0136

Shen, Q., Zhong, L., & Hu, H. F. (2004). Characterization of the surface properties of xylan by FT-Raman spectroscopy and wicking technique. *Colloids and Surfaces B-Biointerfaces, 39*(4), 195–198. https://doi.org/10.1016/j.colsurfb.2004.10.003

Shi, M. C., Gao, Q., Rao, J., Lv, Z. W., Chen, M. X., Chen, G. G., … Peng, F. (2023). Confinement-modulated clusterization-triggered time-dependent phosphorescence color from xylan-carbonized polymer dots. *Journal of the American Chemical Society, 146*(2), 1294–1304. https://doi.org/10.1021/jacs.3c07034

Sorolla-Rosario, D., Llorca-Porcel, J., Perez-Martinez, M., Lozano-Castello, D., & Bueno-Lopez, A. (2022). Study of microplastics with semicrystalline and amorphous structure identification by TGA and DSC. Journal of Environmental. *Chemical Engineering, 10*(1). https://doi.org/10.1016/j.jece.2021.106886

Su, L., Feng, Y. L., Wei, K. C., Xu, X. Y., Liu, R. Y., & Chen, G. S. (2021). Carbohydrate-based macromolecular biomaterials. *Chemical Reviews, 121*(18), 10950–11029. https://doi.org/10.1021/acs.chemrev.0c01338

Teleman, A., Larsson, P. T., & Iversen, T. (2001). On the accessibility and structure of xylan in birch kraft pulp. *Cellulose, 8*(3), 209–215. https://doi.org/10.1023/a:1013195030404

Thomas, B., Raj, M. C., Athira, K. B., Rubiyah, M. H., Joy, J., Moores, A., … Sanchez, C. (2018). Nanocellulose, a versatile green platform: From biosources to materials and their applications. *Chemical Reviews, 118*(24), 11575–11625. https://doi.org/10.1021/acs.chemrev.7b00627

Torres-Rendon, J. G., Schacher, F. H., Ifuku, S., & Walther, A. (2014). Mechanical performance of macrofibers of cellulose and chitin nanofibrils aligned by wet-stretching: A critical comparison. *Biomacromolecules, 15*(7), 2709–2717. https://doi.org/10.1021/bm500566m

Urbanowicz, B. R., Peña, M. J., Moniz, H. A., Moremen, K. W., & York, W. S. (2014). Two Arabidopsis proteins synthesize acetylated xylan *in vitro*. *Plant Journal, 80*(2), 197–206. https://doi.org/10.1111/tpj.12643

Vibert, C., Fayolle, B., Ricard, D., & Dupont, A. L. (2023). Decoupling hydrolysis and oxidation of cellulose in permanent paper aged under atmospheric conditions. *Carbohydrate Polymers, 310*. https://doi.org/10.1016/j.carbpol.2023.120727

Wang, H. R., Li, X. P., Zhao, S. W., Liu, Q. L., Li, N., Su, Z. H., … Peng, F. (2023). Repurposing xylan biowastes for sustainable household detergents. *ACS Sustainable Chemistry & Engineering*. https://doi.org/10.1021/acssuschemeng.2c06439

Wang, S. Y., & Xiang, Z. Y. (2021). Highly stable pickering emulsions with xylan hydrate nanocrystals. *Nanomaterials, 11*(10). https://doi.org/10.3390/nano11102558

Wang, Y., Azhar, S., Lindstrom, M. E., & Henriksson, G. (2015). Stabilization of polysaccharides during alkaline pre-treatment of wood combined with enzyme-

supported extractions in a biorefinery. *Journal of Wood Chemistry and Technology, 35* (2), 91–101. https://doi.org/10.1080/02773813.2013.875041

Xie, R. X., Weisen, A. R., Lee, Y., Aplan, M. A., Fenton, A. M., Masucci, A. E., … Gomez, E. D. (2020). Glass transition temperature from the chemical structure of conjugated polymers. *Nature. Communications, 11*(1). https://doi.org/10.1038/s41467-020-14656-8

Xu, S., Chen, R. F., Zheng, C., & Huang, W. (2016). Excited state modulation for organic afterglow: Materials and applications. *Advanced Materials, 28*(45), 9920–9940. https://doi.org/10.1002/adma.201602604

Yang, C. N., Hung, K. C., Wu, T. L., Yang, T. C., Chen, Y. L., & Wu, J. H. (2014). Comparisons and characteristics of slicewood acetylation with acetic anhydride by liquid phase, microwave, and vapor phase reactions. Bioresources, 9(4), 6463–6475, Retrieved from <Go to ISI>://WOS:000345396900057.

Yang, H. Y., Song, X. L., Yuan, T. Q., Xu, F., & Sun, R. G. (2011). Fractional characterization of hemicellulosic polymers isolated from Caragana korshinskii Kom. *Industrial & Engineering Chemistry Research, 50*(11), 6877–6885. https://doi.org/10.1021/ie1016738

Yundt, A. P. (1949). Crystalline xylan and mannan. *Journal of the American Chemical Society, 71*(2), 757–758. https://doi.org/10.1021/ja01170a525

Zhang, H. Y., Johnson, A. M., Hua, Q., Wu, J., Liang, Y. L., Karaaslan, M. A., … Renneckar, S. (2023). Size-controlled synthesis of xylan micro/nanoparticles by self-assembly of alkali-extracted xylan. *Carbohydrate Polymers, 315*. https://doi.org/10.1016/j.carbpol.2023.120944

Zhu, J. J., Tian, Y. L., Liu, X. P., & Yang, C. J. (2019). Lithography-induced hydrophobic surfaces of silicon wafers with excellent anisotropic wetting properties. *Microsystem Technologies-Micro-and Nanosystems-Information Storage and Processing Systems, 25* (2), 735–745. https://doi.org/10.1007/s00542-018-4010-3

Zuza, E., Ugartemendia, J. M., Lopez, A., Meaurio, E., Lejardi, A., & Sarasua, J. R. (2008). Glass transition behavior and dynamic fragility in polylactides containing mobile and rigid amorphous fractions. *Polymer, 49*(20), 4427–4432. https://doi.org/10.1016/j.polymer.2008.08.012